Journal of Zhejiang University-SCIENCE A (Applied Physics & Engineering) 2022 23(8):587-598
www.jzus.zju.edu.cn; www.springer.com/journal/11582
E-mail: jzus_a@zju.edu.cn

Research Article
https://doi.org/10.1631/jzus.A2100375

Design and friction loss study of full-ocean depth oil-filled direct current motor

Hao WANG, Chen CAO, Jin GUO, Wei WANG, Peng ZHOU, Jia-wang CHEN✉

Ocean College, Zhejiang University, Zhoushan 316000, China

Abstract: In this study, we designed an oil-filled motor that can be used at full-ocean depths, and investigated the friction losses caused by the rotating seal and the properties of the oil. The direct current (DC) motor is encapsulated in an aluminum alloy housing. A rubber diaphragm is used to balance the internal and external pressures so that the motor can work on the seabed without pressure difference. To study the resistance caused by the rotating seal, a numerical model of the Glyd ring and the rotating shaft was established. Results from a rotational torque test agreed with those from numerical analysis. The kinematic viscosity of four oils was measured at 1–25 °C. Oil bath experiments in an incubator showed that the resistance from oil is highly correlated with its dynamic viscosity. Dimethicone appears to be very suitable as an insulating oil for these motors. The working characteristics of the motor were tested in a high-pressure chamber. The results showed that the motor needs to overcome higher oil resistance under higher pressure. A prototype of a pressure-adaptive motor was designed and applied successfully in the hadal zone at a water depth of more than 10000 m.

Key words: Oil-filled motor; Full-ocean depth; Rotating seals; Friction loss; Viscous power; Sea trial

1 Introduction

Direct current (DC) motors have the advantages of a high power to density ratio, strong overload capacity, convenient speed regulation, and low cost. They are widely used as drives in marine engineering applications including pipeline lifting systems (Kang et al., 2019), weight adjustment systems of manned submersibles (Qiu, 2008), and the dynamic thruster systems of deep-water vehicles (Li et al., 2009; Meng, 2021). Deep-sea DC motors are used in monitoring systems (Smith and Teal, 1973) and deep-sea samplers (Zhang et al., 2012; Chen et al., 2020; Wang et al., 2020).

Deep-water motors transmit torque to the outside via a magnetic coupling or a shaft with a rotating seal (Fu et al., 2019; Gasparoto et al., 2021). When working in shallow water, the isolation sleeve of the magnetic coupling motor is thin. This mimimizes the impact on the motor's magnetic field, making the motor highly efficient. However, as the water depth increases, the shell and the isolation sleeve must be thickened to withstand the hydrostatic pressure, resulting in more current loss caused by eddies. The efficiency of this type of motor is therefore severely reduced. The cabin of an oil-filled motor is filled with insulating oil and uses a pressure compensation structure to balance the inside and outside pressures on the motor. Therefore, a thick shell is no longer required, allowing a significant reduction in the weight of the motor. The oil also cools other parts inside the motor and reduces mechanical vibration and noise. Thus, an oil-filled motor is a low-cost and efficient deep-sea actuator.

Researchers have extensively studied the performance of oil-filled motors, including their heat generation effects, viscous losses, starting characteristics, mechanical losses, and parameter optimization design (Li et al., 2010; Xu et al., 2010; Cai et al., 2016; Bai et al., 2018; Romanov and Goldstein, 2018). Frictional losses in deep-sea oil-filled motors arise mainly from rotating seals and viscosity (mechanical losses

✉ Jia-wang CHEN, arwang@zju.edu.cn
Hao WANG, https://orcid.org/0000-0001-7757-3753
Jia-wang CHEN, https://orcid.org/0000-0002-6351-0062

Received Aug. 5, 2021; Revision accepted Feb. 25, 2022;
Crosschecked June 30, 2022

are not discussed here). There have been many studies on the viscous power of oil-filled motors. The experimental results show that the viscous power of a high-power motor with a total capacity of 60 kW is about 6 kW when operating at 60 MPa at 2 °C. In contrast, the viscous power is only 0.5 kW under usual working conditions (ambient conditions) (Umapathy et al., 2019). The viscous power of a small DC brushless oil-filled motor at 70 MPa exceeds atmospheric pressure by 51.4% (Zou et al., 2012). Researchers at Zhejiang University, China studied the starting characteristics and viscous losses of oil-filled motors at 2–25 °C and 0.1–60.0 MPa, and derived an empirical formula for calculating viscous losses. In more complex cases, such as motors for deep-sea electric manipulators, more sophisticated numerical calculation models were developed to consider the effects of grooves on the stator and rotor surfaces. The surface grooves were filled with epoxy resin to optimize the geometry of the gap. Experiments showed that this approach can effectively reduce the viscosity loss of the motor (Bai et al., 2021).

While the viscous loss of oil-filled motors is a current focus of research, there is a lack of research at depths over 7000 m (hydrostatic pressure above 70 MPa). In addition, there have been few studies on the evaluation of the friction loss and sealing performance of seals of the rotating shaft of oil-filled motors. With the rapid development of deep-sea exploration technology, the hadal zone has become the frontier of marine science (Du et al., 2021). As an important actuator, the performance of an oil-filled motor in the hadal needs further analysis. The purpose of this study was to propose a detailed design of an oil-filled motor that can be applied at full-ocean depth, focusing on rotating seal losses and viscous losses. Multiple applications of this motor in the Marianas Trench are given.

2 Design of the motor

2.1 Mechanical structure

Fig. 1 shows the detailed structure of the full-ocean depth oil-filled DC brushless motor (AM-BL45100AN, Zhengyuan Co., Ltd., China). When the motor is equipped with a reducer (AM 45GP, Zhengyuan Co., Ltd.), the maximum torque can reach more than 30 N·m. There are three vents on the sidewall of the shell: two for filling the motor with oil, and another for a 4-pin waterproof plug. The motor shell is made of aluminum alloy 6061T6 with oxidation treatment on the surface. This alloy has high strength and low density, which satisfy the requirements of lightweight and corrosion resistance for deep-sea equipment. The rotation shaft is made of stainless steel 316. The deformation of the rubber diaphragm balances the internal and external pressures and ensures that there is no pressure difference between each side of the combined sealing ring. The control circuit board of the motor has high-pressure resistant components (capacitors, chips, etc.), and is installed in the motor control cabin. The designed motor has a total length of 340 mm and an underwater weight of 1.2 kg, and can be easily installed in deep-sea equipment.

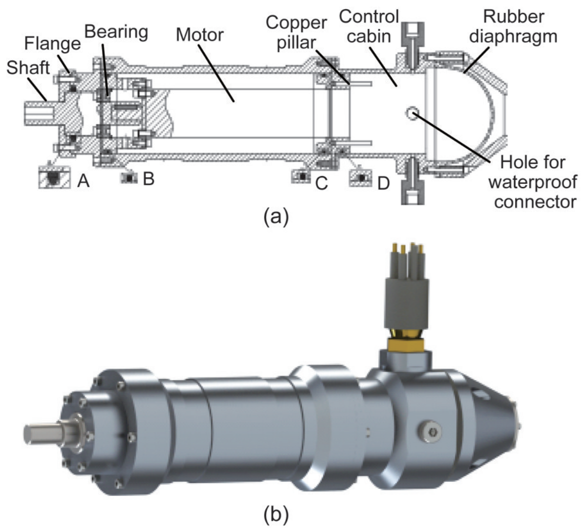

Fig. 1 Structure of the oil-filled motor: (a) detailed structure; (b) 3D model of the motor. A: rotating seal; B, C, and D: static seals

To guarantee the production processing quality, the form and position errors of geometric features of the parts need to be restricted within a tolerance range. The characteristics of form and position errors include geometric size, the scope of changes, and the direction and position of the parts. According to the Pareto principle, a few key condition factors cause most of the tolerance fluctuations. In the production process, the variation of geometric parameters is controlled within the tolerance fluctuation range by adjusting these critical condition factors.

2.2 Control and work mode

The control of the motor is realized by the method shown in Fig. 2a. The central control module can control two motors at the same time. The central control module communicates with the motor in real time, and the motor's communication module controls the motor's drive module to start or stop the motor. The control software of the motor (Fig. 2b) can control the motor manually or automatically. Usually, when operating at deep-sea levels, we set the working mode to automatic. The delay start time interval, forward rotation time, reverse rotation time, etc., are set in the automatic control module of the software, with specific parameters depending on the requirements of the operation.

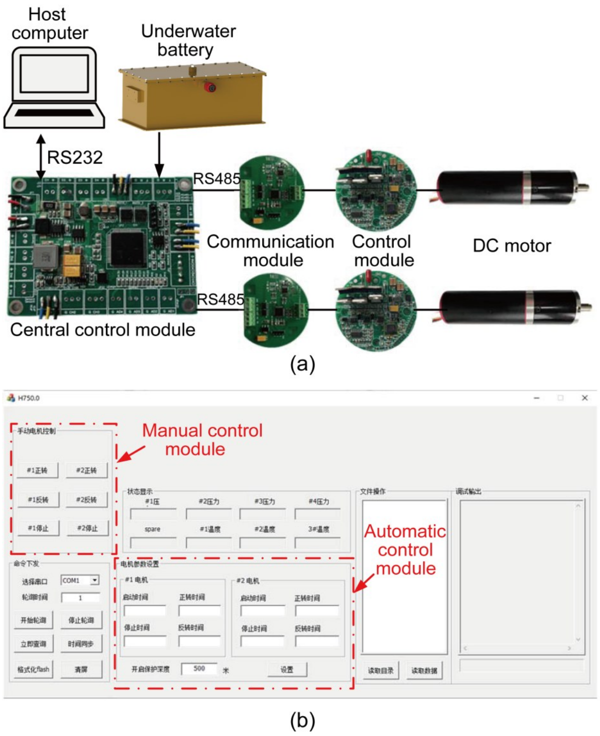

Fig. 2 Control and interface of the software: (a) control system; (b) interface of the software

3 Friction of the rotating seal

3.1 Simulation model

To solve the rotating seal friction, we first obtained the contact pressure distribution and contact length by simulation. Then, the normal force and total friction torque on the entire contact surface were obtained by integration. The combined seal component exerts a radial contraction force on the slip ring through O-ring compression. Specific contact stress is generated between the slip ring and the drive shaft, which seals the motor. The O-ring can compensate for the wear of the slip ring to a certain extent.

We studied the contact pressure distribution characteristics of various forms of rubber O-ring–PTFE (polytetrafluoroethylene) square ring combined seals under different degrees of interference installation conditions with the drive shaft. A numerical analysis model was built, using the finite element analysis software Abaqus, to study the contact stress distribution (Fig. 3). The total number of grids was 4632 and the approximate unit size was 0.08 mm. A CAX4R unit was used for the slip ring, sleeve, and driveshaft. The O-ring adopted the CAX4RH unit to adapt to large deformation characteristics. Since the deformation of the sleeve and the drive shaft can be ignored compared to the deformation of the O-ring and the slip ring, they are set as rigid bodies. The diameter of the O-ring was 3.55 mm, and the width of the groove was 5.00 mm. A penalty function model described each contact type, and the friction factor of each contact pair was defined as shown in Table 1. Interference installation was adopted between the O-ring and the sleeve. We set the interference amount to 5%, 10%, 15%, 20%, 25%, or 30%.

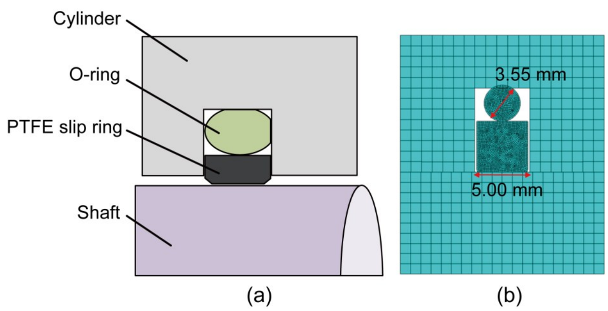

Fig. 3 Geometry (a) and mesh (b) of the numerical analysis model

Table 1 Definition of contact pairs in the model

Contact pair	Contact type	Slide setting	Friction coefficient
Shaft–slip ring	Surface to surface	Small	0.15
Slip ring–O-ring	Node to surface	Finite	0.50
O-ring–cylinder	Node to surface	Finite	0.50

The stress-strain properties of the rubber material were tested by uniaxial tension. The Mooney-Rivlin constitutive model parameters were calculated using the material evaluation function in Abaqus. The parameter C10 was 1.87, and the parameter C01 was 0.47. Other materials were described by linear models, and their material parameter settings are shown in Table 2.

3.2 Simulation results

The contact path of the slip ring and the drive shaft was established in the post-processing module of Abaqus. The maximum contact stress was located at the contact point between the two ends of the slip ring and the drive shaft. The contact stress decreased rapidly towards the middle part, and then fluctuated around a fixed value. As the compression ratio of the O-ring increased linearly, this stable value showed a greater increase. MATLAB software was used to fit the curve and obtain the corresponding equations (Fig. 4).

The contact pressure between the sealing surface of the shaft and the slip ring can be expressed as

$$F=\int_0^b \pi D y \mathrm{d}x, \tag{1}$$

where F is the contact pressure, b is the actual contact surface width, D is the diameter of the rotating shaft, and y is the fitting equation.

Table 2 Material parameter settings

Part	Material	Density (g/cm^3)	Young's modulus (MPa)	Poisson's ratio
Cylinder	Aluminum alloy 6061T6	2.7	72000	0.33
Shaft	Stainless steel 316	7.9	210000	0.26
Slip ring	PTFE	2.3	960	0.45

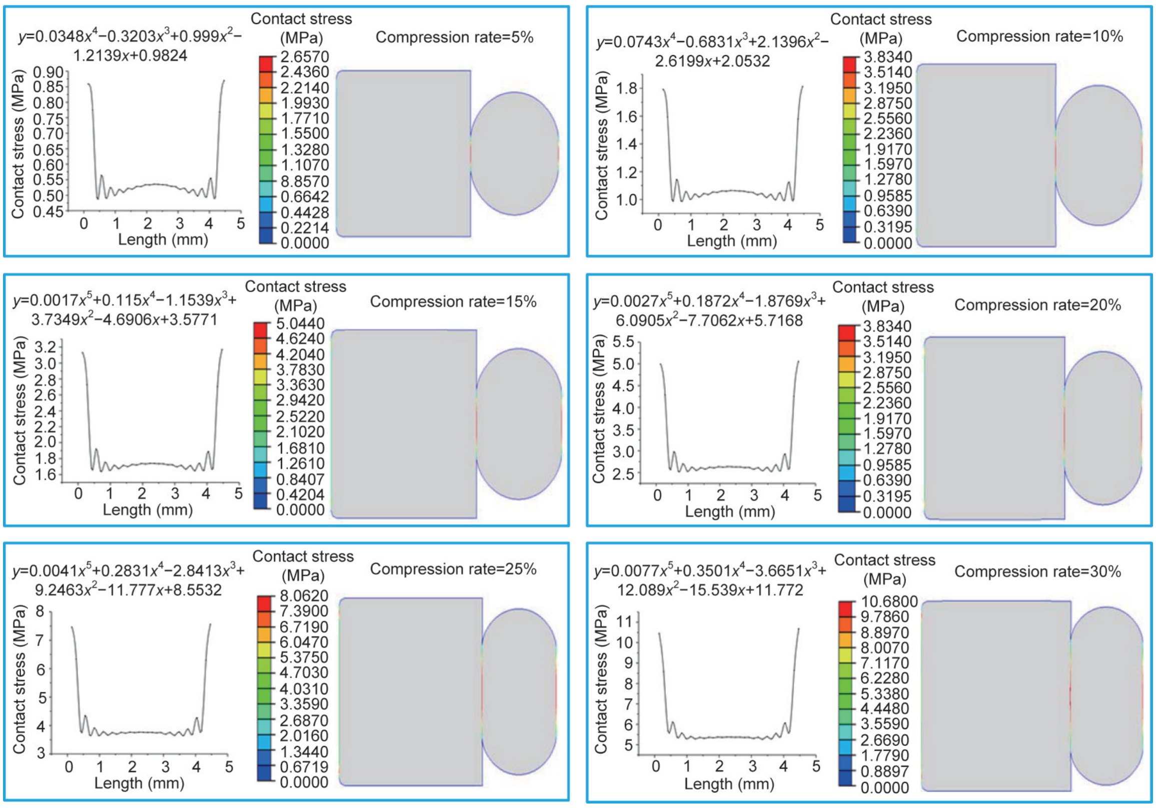

Fig. 4 Contact distributions under different compression rates

The friction torque can be expressed as

$$T=F\frac{D}{2}\mu, \tag{2}$$

where T is the friction torque, and μ is the friction factor, which was 0.15.

The results of the friction torque under different compression ratios are shown in Table 3.

Table 3 Friction torque calculation results

Compression rate	Friction torque (N·m)
5%	0.155
10%	0.312
15%	0.515
20%	0.781
25%	1.119
30%	1.602

3.3 Torque test

To validate the simulation results, a torque test platform was built (Fig. 5).

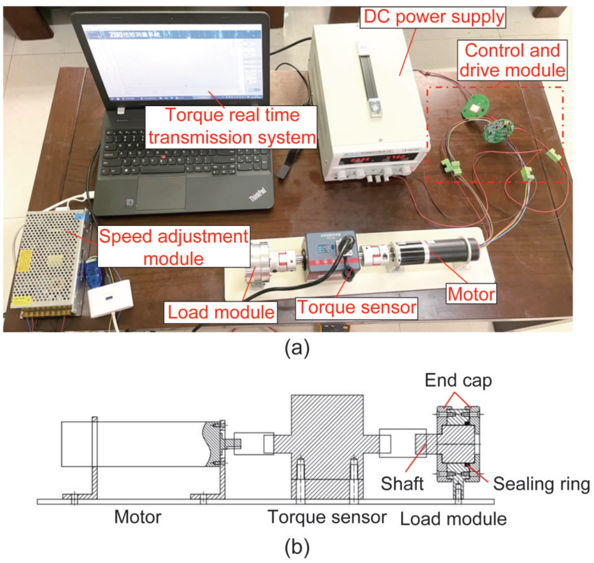

Fig. 5 Torque test platform: (a) test platform; (b) detailed structure

The experimental results (Table 4) showed that as the compression ratio increased, the starting torque increased sharply, and the maximum of the start torque was more than 2.5 times greater than the stable torque. Here, the starting torque refers to the moment at the beginning of each set of experiments. The stable torque exceeded the calculation results by 20%–30%. This discrepancy is related to the accuracy of surface machining, the power loss of the coupling, and the power loss of the reducer. These factors were not taken into account in the theoretical calculations. Therefore, this is a reasonable calculation method, as the experiment results were generally greater than the calculation results.

Table 4 Torque test results

Compression rate	Start torque (N·m)	Stable torque (N·m)
5%	0.3270	0.18755
10%	0.5608	0.37752
15%	1.1510	0.62315
20%	2.6554	0.94501
25%	3.8046	1.35399
30%	5.4468	1.93842

When an oil-filled motor works on the seabed, there may be a small amount of leakage due to the movement of the rotating shaft. Therefore, we considered compressing the bladder to a certain extent before deployment, so that the pressure inside the motor was slightly greater than that outside (not exceeding 1 MPa). When the motor works on the seabed, even if there is a small amount of leakage, no seawater will enter the motor compartment, but oil may leak into the seawater. We chose the size of the sealing ring to match the groove with a compression rate of 15%. The average contact pressure was greater than 1.6 MPa under this combination, which can meet the sealing requirements and avoid excessive frictional resistance resulting in excessive power consumption.

4 Influence of oil

4.1 Influence of temperature

As the temperature decreases, the viscosity of the hydraulic oil increases significantly (Fig. 6). The viscosity of the silicone oil also increases, but the change is relatively small.

After consulting the manufacturer for the internal structural parameters of the motor, we established a numerical analysis model (Fig. 7). The hydrodynamic characteristics of the motor rotating at different speeds in different liquid media were analyzed, based on the shear stress transfer (SST) k-ω turbulence model in the Reynolds-averaged Navier-Stokes equations (RANS) and the slip mesh technique in Fluent. The k-ω model shows good performance in predicting the flow and separation of the adverse pressure gradient boundary layer, and it is widely used in the hydrodynamic analysis for rotating machinery, such as propellers. The slip mesh technique can accurately solve rotor-stator interactions in transient analysis mode when dealing with problems that do not involve mesh deformation (Ji et al., 2012; Dubbioso et al., 2014). Fig. 7 shows a schematic diagram of the internal chamber of the motor. The rotating shaft is divided into a hexahedral structured mesh, and a boundary layer mesh is divided on its surface (the mesh thickness is 0.1 mm). The stator part is divided into an unstructured mesh due to its complex structure. The total number of grids is 612288 and the maximum size is 0.8 mm. The results are shown in Fig. 8.

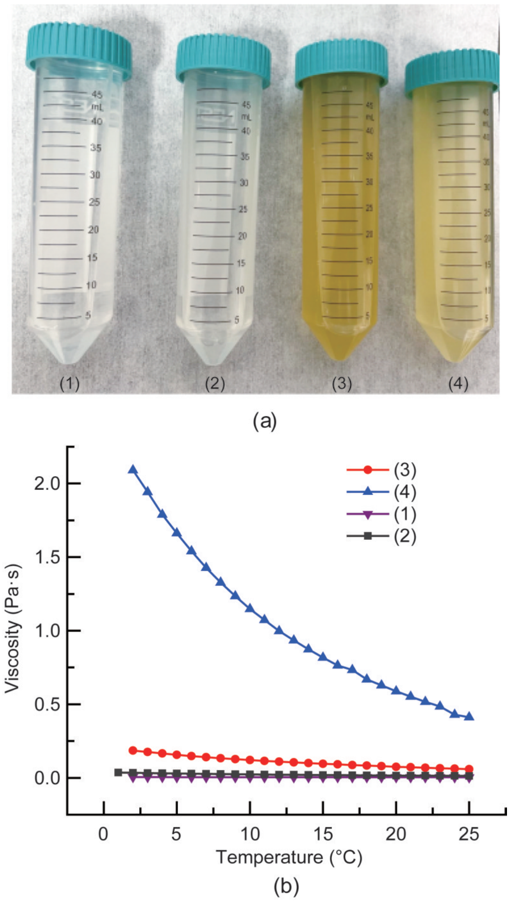

Fig. 6 (a) Four tested types of oil: dimethyl silicone oil (1) (GB-3881, Bogang Co., Ltd., China), diethyl silicone oil (2) (DC-1785, Kaiyin Co., Ltd., China), and hydraulic oils (3) and (4) (DTE Excel Series and HVI26, Mobil Co., Ltd., the USA); (b) viscosity of the oils

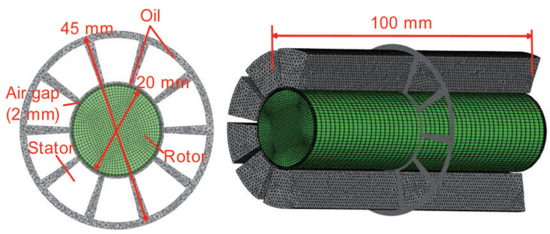

Fig. 7 Simulation model of the internal chamber of the motor

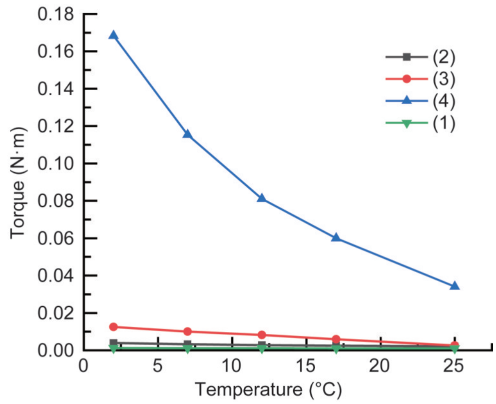

Fig. 8 Simulation results

The motor was placed in an oil bath in a temperature-controlled testing box. Due to the size limitations of the box, we could not place the load into the box simultaneously. Therefore, we used the working current of the motor to describe the viscous resistance approximately (Fig. 9). There was a high correlation between the operating current and the viscosity of the oil at different temperatures. Temperatures exceeding 10 °C had little effect on the operating current of the motor. However, the temperature of the deep sea is generally 2–4 °C, and the oil-filled motor was obviously affected by temperatures in this range. We chose oil (1) to fill our motor.

4.2 Influence of pressure

The purpose of the test shown in Fig. 10 was to study the performance of the oil-filled motor under high pressure. Because the torque sensor cannot be used in water and high-pressure environments, we placed the motor in a high-pressure chamber and analyzed its working characteristics through its current.

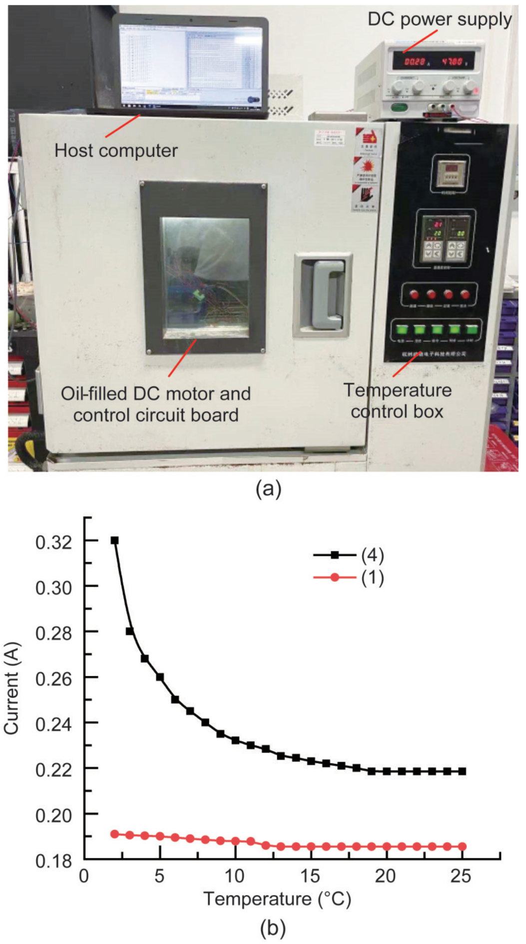

Fig. 9 Temperature test: (a) test box; (b) working current of the motor

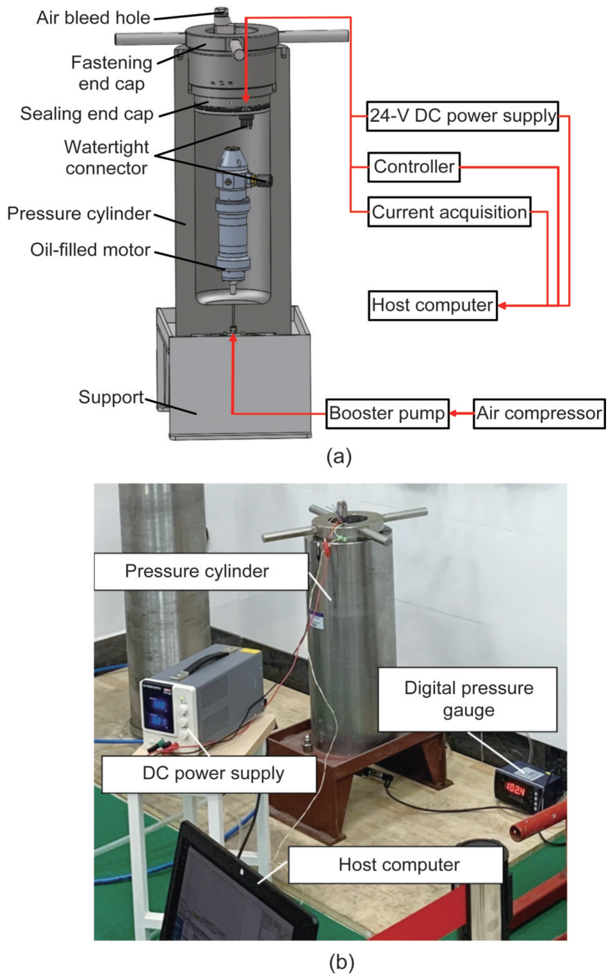

Fig. 10 High-pressure test

The relationship between torque and current can be expressed as

$$M = k_M I_M, \tag{3}$$

where M is the mechanical torque, k_M is the torque constant, and I_M is the current.

The relationship between the internal friction torque of the motor and the no-load current can be expressed as

$$M_R = k_M I_0, \tag{4}$$

where M_R is the internal friction torque of the motor, and I_0 is the idling current.

The efficiency of the motor can be expressed as

$$\eta_1 = \frac{\pi}{30000} \frac{n_1 (M - M_R)}{U_M I_M}, \tag{5}$$

where η_1 is the efficiency of the motor, n_1 is the output speed of the motor, and U_M is the voltage.

Then, the output power of the motor is defined as follows:

$$P_1 = \frac{\pi}{30000} \eta_1 (M - M_R). \tag{6}$$

The input power of the reducer is equal to the output power of the motor, and the output power of the reducer can be expressed as

$$P_2 = P_1 \eta_2 = \frac{\pi}{30000} n_2 M_2, \tag{7}$$

where M_2 is the output torque of the reducer, n_2 is the output speed of the reducer, and η_2 is the efficiency of the reducer.

When $i=n_1/n_2$, the output torque of the reducer is defined as follows:

$$M_2=k_M i\eta_2(I_M-I_0). \tag{8}$$

The characteristic parameters k_M, i, η_2, and I_0 of the motor we selected can be obtained from the motor selection manual, and their values are shown in Table 5.

Table 5 Characteristic parameters of the motor

Parameter	Value
k_M (N·m/A)	0.076
i	104
η_2	0.72
I_0 (A)	0.19

Substituting the above parameters into the formula gives

$$M_2=5.691I_M-1.081. \tag{9}$$

The pressure was increased from 0 MPa in 10-MPa increments, and the pressure rate was 0.5 MPa/min. Each time the pressure was increased, the motor was controlled to start. The motor worked for 20 min each time, and the current value was recorded after stabilization (Table 6). In the process of pressure relief, the rate of pressure drop was controlled to be 0.5 MPa/min. This was to prevent damage to the motor, especially its internal controller, due to an excessive rate of pressure drop.

Table 6 High-pressure test current

Pressure (MPa)	Stable current (A)	Torque (N·m)
0	0.31	0.68321
10	0.33	0.79703
20	0.34	0.85394
30	0.36	0.96776
40	0.38	1.08158
50	0.41	1.25231
60	0.45	1.47995
70	0.52	1.87832
80	0.61	2.39051
90	0.68	2.78888
100	0.74	3.13034
110	0.90	4.04090
120	1.05	4.89455

Analysis of the calculation results showed that up to 60 MPa, the output torque had an approximately linear relationship with the increase in pressure. When the pressure exceeded 70 MPa, the increase in output torque was significantly increased. This is related to the change of the viscosity of the oil under high pressure and the change of the motor speed. Therefore, the motor needs to overcome a greater loss of friction under ultra-high pressure.

5 Application and sea trial of the motor

5.1 60-MPa high-pressure chamber test

During the 60-MPa hyperbaric chamber test, several sets of deep-sea sampling equipment were placed on the support (Fig. 11). Three sets of full-sea depth sampling equipment, A, B, and C, were deployed, all of which use the pressure-balanced full-sea depth oil-filled DC motor developed by this research as the driving device. The operation of the oil-filled motor was controlled by an electronic chamber, and the control program was written into the central control module before deployment. The chamber was equipped with lights and cameras so that the working conditions of the equipment could be observed outside. The actions of sampling devices A and B during the hyperbaric chamber test are shown in Figs. 12 and 13, respectively (because the only movement of sampling device C that could be observed by the camera was the rotation of the shaft, this action is not shown).

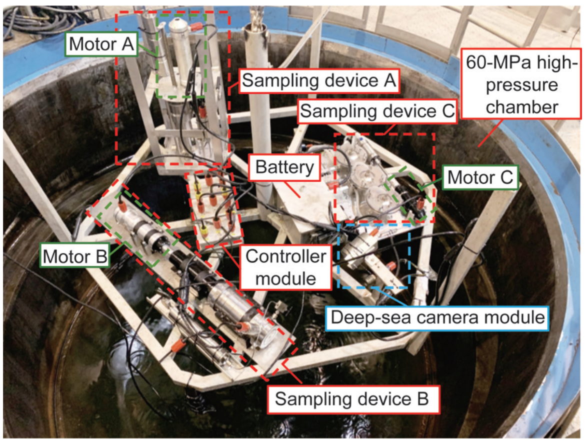

Fig. 11 60-MPa high-pressure chamber test

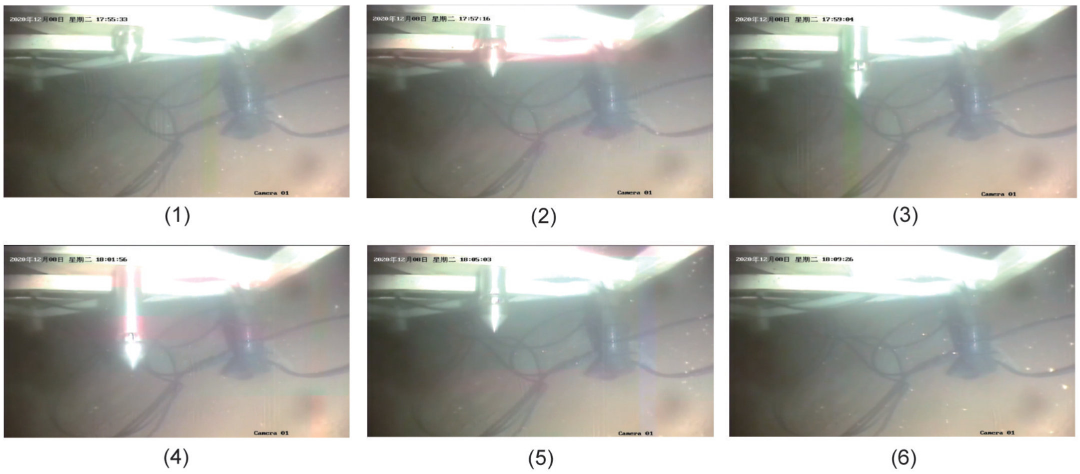

Fig. 12 Action process of sampling device A in the 60-MPa high-pressure chamber at different times (1)–(6)

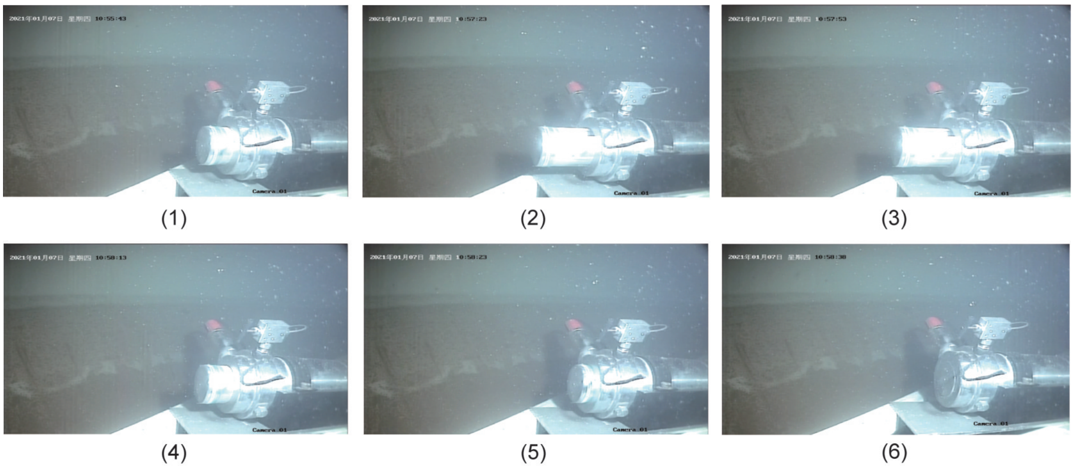

Fig. 13 Action process of sampling device B in the 60-MPa high-pressure chamber at different times (1)–(6)

Both sampling devices were started according to the presupposed time and reversed to drive the sampling mechanism to complete a reciprocating movement process.

5.2 In-situ application

The developed oil-filled motors are equipped as actuators on many deep-sea instruments (Fig. 14). Multiple applications in the Marianas Trench have demonstrated that the motors can operate in the deepest extreme environments of the ocean.

6 Conclusions and discussion

With the development of deep-sea exploration technology, oil-filled DC motors will become important actuators. The designed motor has completed several operational tasks at depths of over 11000 m, which shows that the motor can operate at full-sea depth. The developed pressure balancing mechanism, motor control system, and upper computer software make our motor very easy to use and suitable for a wide range of applications.

However, the developed motor still has some shortcomings: (1) We found that the rubber diaphragm of the oil-filled motor would rupture after several working operations on the seabed, probably because the rubber material selected could not withstand repeated cyclic loads. (2) The motor is unsuitable for high-speed operation because the rotating seal will leak at high speed. (3) Sometimes, the motor starts up on the seafloor with a lag or advance of up to 15% over the set time.

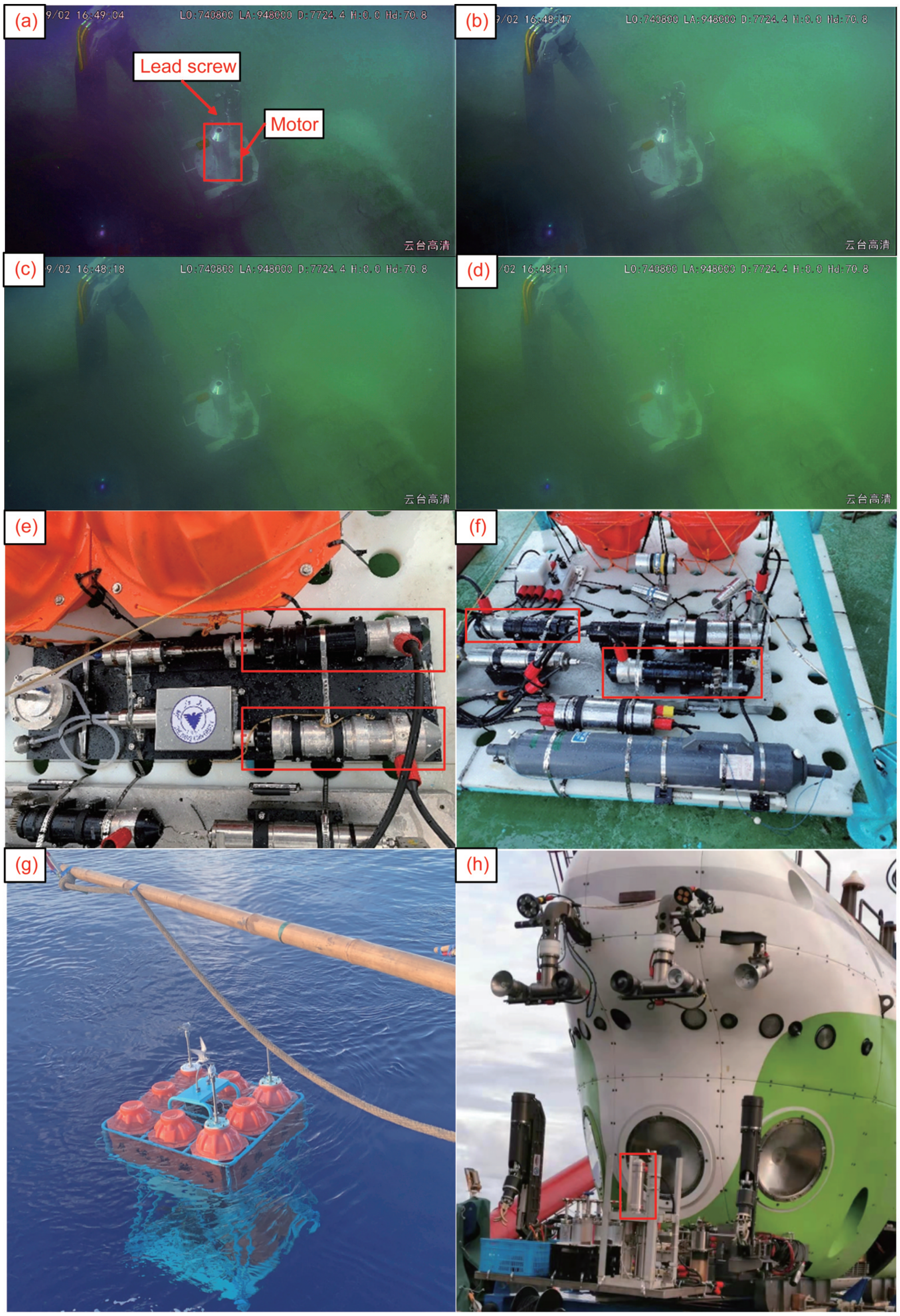

Fig. 14 In-situ applications of the motor: (a–d) motor driving a sediment sampler at the bottom of the Mariana Trench to acquire samples; (e) motor deployed on a filter device; (f) motor deployed on a benthic capture device; (g) motor mounted on the "Yuanweishiyanhao" lander for testing; (h) motor mounted on the "Fendouzhe" manned submersible for testing

Therefore, we believe that future research on deep-sea motors should focus on the following aspects: (1) development of unique materials, such as oil and rubber diaphragms dedicated to deep-sea oil-filled motors; (2) development of more accurate motor control methods; (3) development of new sealing structures for deep-sea electromechanical devices, such as the silica gel seal used by some designers (Li et al., 2021), which can reduce the weight of the device.

Acknowledgments

This study is supported by the National Key R&D Program of China (No. 2018YFC0310601), the Strategic Priority Research Program of the Chinese Academy of Science (No. XDA22000000), the National Key Research and Development Program of China (Nos. 2016YFC0300800 and 2017YFC006500), and the Key Program of Sanya Yazhouwan, China. We are grateful to the team of the Yuanweishiyan LANDER, and the pilots, captain, and crews of the R/V Tansuoyihao for their professional service during the TS-21 cruises organized by the Institute of Deep-sea Science and Engineering, Chinese Academy of Sciences.

Contributors

Hao WANG mainly designed the device. Hao WANG and Jia-wang CHEN processed the data. Hao WANG and Chen CAO drafted the manuscript. Jin GUO, Wei WANG, and Peng ZHOU helped to organize the manuscript. Peng ZHOU helped to design the device.

Conflict of interest

Hao WANG, Chen CAO, Jin GUO, Wei WANG, Peng ZHOU, and Jia-wang CHEN declare that they have no conflict of interest.

References

Bai YF, Zhang QF, Fan YL, et al., 2018. Research and experiment on viscous friction power loss of deep-sea electric manipulator. Proceedings of OCEANS-MTS/IEEE Kobe Techno-Oceans, p.1-4. https://doi.org/10.1109/OCEANSKOBE.2018.8559121

Bai YF, Zhang QF, Zhang AQ, 2021. Modeling and optimization of compensating oil viscous power for a deep-sea electric manipulator. *IEEE Access*, 9:13524-13531. https://doi.org/10.1109/ACCESS.2021.3052165

Cai MJ, Wu SJ, Yang CJ, 2016. Effect of low temperature and high pressure on deep-sea oil-filled brushless DC motors. *Marine Technology Society Journal*, 50(2):83-93. https://doi.org/10.4031/MTSJ.50.2.8

Chen JW, Huang Y, Lin Y, et al., 2020. A novel sediment pressure sampling device carried by a hadal-rated lander. *Journal of Marine Science and Engineering*, 8(11):839. https://doi.org/10.3390/jmse8110839

Du MR, Peng XT, Zhang HB, et al., 2021. Geology, environment, and life in the deepest part of the world's oceans. *The Innovation*, 2(2):100109. https://doi.org/10.1016/j.xinn.2021.100109

Dubbioso G, Muscari R, di Mascio A, 2014. Analysis of a marine propeller operating in oblique flow. Part 2: very high incidence angles. *Computers & Fluids*, 92:56-81. https://doi.org/10.1016/j.compfluid.2013.11.032

Fu M, Yan H, Yin ZY, et al., 2019. Coupling calculation of 3D whole domain steady flow and temperature field for underwater oil-filled brushless DC motors. Proceedings of the 22nd International Conference on Electrical Machines and Systems, p.1-6. https://doi.org/10.1109/ICEMS.2019.8922073

Gasparoto HF, Chocron O, Benbouzid M, et al., 2021. Advances in reconfigurable vectorial thrusters for adaptive underwater robots. *Journal of Marine Science and Engineering*, 9(2):170. https://doi.org/10.3390/jmse9020170

Ji B, Luo XW, Peng XX, et al., 2012. Numerical analysis of cavitation evolution and excited pressure fluctuation around a propeller in non-uniform wake. *International Journal of Multiphase Flow*, 43:13-21. https://doi.org/10.1016/j.ijmultiphaseflow.2012.02.006

Kang YJ, Liu SJ, Zou WS, et al., 2019. Design and analysis of an innovative deep-sea lifting motor pump. *Applied Ocean Research*, 82:22-31. https://doi.org/10.1016/j.apor.2018.10.018

Li GR, Chen XP, Zhou FH, et al., 2021. Self-powered soft robot in the Mariana trench. *Nature*, 591(7848):66-71. https://doi.org/10.1038/s41586-020-03153-z

Li JJ, Xu YX, Zou JB, et al., 2009. Rotor eddy-current loss of permanent magnet machine in brushless AC and DC modes, used for deep-sea HUV's propeller. Proceedings of the International Conference on Electrical Machines and Systems, p.1-4. https://doi.org/10.1109/ICEMS.2009.5382701

Li JJ, Zhou JB, Jiang XT, et al., 2010. Electrical-thermal coupled calculation of a submersible motor used for deep-sea electromagnetic propeller. Proceedings of the Digests of the 14th Biennial IEEE Conference on Electromagnetic Field Computation, p.1. https://doi.org/10.1109/CEFC.2010.5481401

Meng JH, 2021. Sliding mode variable structure chaos control for propulsion motor of deep sea robot. *Journal of Physics: Conference Series*, 2025:012077. https://doi.org/10.1088/1742-6596/2025/1/012077

Qiu ZL, 2008. Design and research on a variable ballast system for deep-sea manned submersibles. *Journal of Marine Science and Application*, 7(4):255-260. https://doi.org/10.1007/s11804-008-7092-y

Romanov VS, Goldstein VG, 2018. The dynamic improvement methods of energy efficiency and reliability of oil production submersible electric motors. *Journal of*

Physics: Conference Series, 944:012099.
https://doi.org/10.1088/1742-6596/944/1/012099

Smith KL, Teal JM, 1973. Deep-sea benthic community respiration: an in situ study at 1850 meters. *Science*, 179(4070): 282-283.
https://doi.org/10.1126/science.179.4070.282

Umapathy A, Babu SM, Vedachalam N, et al., 2019. Influence of deep-sea ambient conditions in the performance of pressure-compensated induction motors. *Marine Technology Society Journal*, 53(1):67-73.
https://doi.org/10.4031/mtsj.53.1.7

Wang H, Chen JW, Wang YH, et al., 2020. Research and analysis of pressure-maintaining trapping instrument for macroorganisms in hadal trenches. *Journal of Marine Science and Engineering*, 8(8):596.
https://doi.org/10.3390/JMSE8080596

Xu YM, Meng DW, Liu YL, et al., 2010. Amelioration research of submersible motor design method. Proceedings of the Asia-Pacific Power and Energy Engineering Conference, p.1-4.
https://doi.org/10.1109/APPEEC.2010.5449324

Zhang X, Luan ZD, Yan J, et al., 2012. Development of a deepsea sediment long coring system based on a Jackhammer for R/V Kexue. Proceedings of the Oceans, p.1-6.
https://doi.org/10.1109/OCEANS.2012.6404782

Zou JB, Qi WJ, Xu YX, et al., 2012. Design of deep sea oil-filled brushless DC motors considering the high pressure effect. *IEEE Transactions on Magnetics*, 48(11):4220-4223.
https://doi.org/10.1109/TMAG.2012.2204731